communications earth & environment

A Nature Portfolio journal

Article

https://doi.org/10.1038/s43247-026-03498-9

Wide-swath satellite altimetry reveals hotspots of small mesoscale eddies in the western Arctic Ocean

Chuanshuai Fu[1,2], Xianxian Han[2], Qiang Wang[2] ✉, Clark Pennelly[1] & Paul G. Myers[1]

Ocean eddies play crucial roles in climate and marine ecosystems. Still, small mesoscale eddies in the climate-sensitive and biologically unique Arctic Ocean remain poorly characterized and understood due to the coarse resolution of traditional gridded altimetry products and sparse in-situ observations. Here, we show that the Surface Water and Ocean Topography satellite mission overcomes these limitations through unprecedented two-dimensional high-resolution measurements of sea level anomalies. We demonstrate this wide-swath satellite altimetry's capability to quantify previously unresolved eddy properties, revealing three persistent hotspots of mesoscale eddies in the southern Beaufort Sea that actively transport low-salinity, heat-retaining, and nutrient-enriched waters from the continental shelf to the interior basin. The observed eddies demonstrate their critical role in shelf-basin exchange while revealing biases in current high-resolution models. These findings advance our understanding of Arctic mesoscale processes and provide essential benchmarks for improving ocean models for this rapidly changing environment.

The western Arctic Ocean hosts the largest Arctic freshwater reservoir[1,2], characterized by the anticyclonic Beaufort Gyre (BG). Its freshwater is primarily supplied by Pacific Water inflows from the Bering Strait, Mackenzie River runoff, and sea ice meltwater[3–5]. A potential release of the accumulated BG freshwater may have far-reaching downstream effects on the North Atlantic Ocean, with profound implications for the global climate systems[6]. Additionally, the Beaufort Sea sustains vital Arctic ecosystems, supporting diverse fish communities and other marine life[7,8].

Abundant mesoscale eddies have been observed in the western Arctic Ocean[9–13]. Eddy activity is found to be one of the crucial mechanisms that regulate freshwater accumulation in the BG region[14,15]. Furthermore, eddies can facilitate the transport of the Alaskan coastal water mass into the deep basin, helping to establish the thermohaline structure and sustain biological productivity in the oligotrophic interior of the Beaufort Sea[16,17]. Moreover, eddies could increase sea ice basal melting through influencing ocean heat fluxes and sea ice advection[18].

In-situ measurements using Ice-Tethered Profilers (ITPs) have been employed to study eddy properties in the Canada Basin, showing that the most commonly detected eddies have relatively small radii, typically ranging from 5 to 10 km, consistent with the small size of the Rossby deformation radius in the region[19,20]. Furthermore, these studies indicate a pronounced dominance of anticyclones over cyclones. However, ITP observations may have a regional sampling bias and cannot examine shallow and smaller eddies (< 5 km), so they do not provide a complete picture of the mesoscale eddy field. Observations from high-resolution spaceborne Synthetic Aperture Radar (SAR) offer valuable information about eddy properties over the open water and marginal ice zone of the western Arctic Ocean[12]. They identify a wider range of surface eddies from 0.5 km to 40–60 km in size. They also show that the number of surface cyclones is double that of anticyclones, contrasting with ITP observations of anticyclonic dominance in halocline eddies[19,20]. These SAR observations suffer from the limited number of SAR images and the underlying biases in the human-supervised eddy detection approach. Automated eddy detection algorithms applied to traditional satellite altimetry data enable statistical characterization of spatial and temporal variability in eddy properties[13,21–23]. However, their coarse resolution does not allow for the detection of small eddies, limiting their applications for the Arctic Ocean.

Most climate models lack the spatial resolution required to resolve Arctic Ocean mesoscale eddies. While a few kilometer-scale ocean models have been developed to simulate eddy dynamics and examine eddy energetics in the Arctic Ocean[24–28], their extreme computational costs limit simulations to short integration periods, restricting their utility to process studies. More importantly, evaluating these high-resolution models depends on the availability of detailed observational eddy statistics—a requirement that has remained largely unfulfilled until now.

---

[1]Department of Earth and Atmospheric Sciences, University of Alberta, Edmonton, AB, Canada. [2]Alfred Wegener Institute, Helmholtz Centre for Polar and Marine Research, Bremerhaven, Germany. ✉e-mail: Qiang.Wang@awi.de

Although observational and modeling challenges have historically hindered progress in investigating the mesoscale eddy field in the Arctic Ocean, this study shows that the advent of the Surface Water and Ocean Topography (SWOT) satellite data marks a breakthrough for mesoscale eddy studies in the western Arctic Ocean's open waters. While SWOT's high resolution of 2 km has proven effective for detecting submesoscale eddies at mid and low latitudes[29,30], we demonstrate its particular suitability for characterizing small mesoscale eddies in the Beaufort Sea, where eddy sizes are constrained by the region's small Rossby deformation radius. Applying an automated eddy detection algorithm to SWOT data, we present the first comprehensive assessment of mesoscale eddy properties and statistics in this region. Our analysis reveals persistent eddy hotspots in the southern Beaufort Sea that play a critical role in cross-shelf transport, facilitating the movement of fresh, warm, and nutrient-enriched Pacific Water and Mackenzie River discharge into the deep basin.

Results

Unprecedented capability to observe Arctic Ocean eddies

Conventional satellite nadir altimeters provide one-dimensional (1D) along-track measurements, requiring data from multiple satellites and subsequent interpolation to construct two-dimensional (2D) global maps of Sea Level Anomalies (SLA). Their coarse resolution in space and time, along with instrument noise, constrain their application for high-latitude ocean studies[31]. The recently launched SWOT mission represents a transformative step forward in our ability to observe and understand ocean dynamics by enabling direct, high-resolution measurements of fine-scale SLA[30,32]. Equipped with the cutting-edge Ka-band Radar Interferometer (KaRIn), SWOT captures two 2D 50 km-wide SLA swaths along the satellite track, with an unprecedented resolution of 2 km[33]. Moreover, it has reached a centimetric accuracy in sea level measurements[34].

Figure 1 illustrates a direct comparison between conventional satellite altimetry and high-resolution SWOT measurements of SLA and mesoscale eddies in the Barrow Canyon Region (BCR) of the Beaufort Sea. Although the gridded daily altimetry product offers a nominal horizontal resolution of 1/8° (~14 km in BCR) through optimal interpolation[35], it can only provide a smoothed representation of ocean surface features, obscuring small-scale dynamic structures (Fig. 1b). It only shows several large eddies with radii larger than ~20 km. In contrast, two SWOT tracks over the same region capture SLA fields at a much finer scale on the same day, resolving smaller coherent eddies (marked by black dots; Fig. 1c). Zoomed-in views showcase their associated geostrophic current anomalies (Fig. 1d and e), unveiling detailed eddy structures and current speeds that were previously undetectable in the conventional gridded altimetry product. This unprecedented resolution highlights SWOT's capability to uncover Arctic eddy dynamics that were once invisible to traditional satellite measurements.

In the Beaufort Sea, SWOT's orbital inclination enables dense coverage and frequent revisits, with ~15 track repeats occurring in the southern Beaufort Sea each month (Fig. 2a). This represents a great improvement in

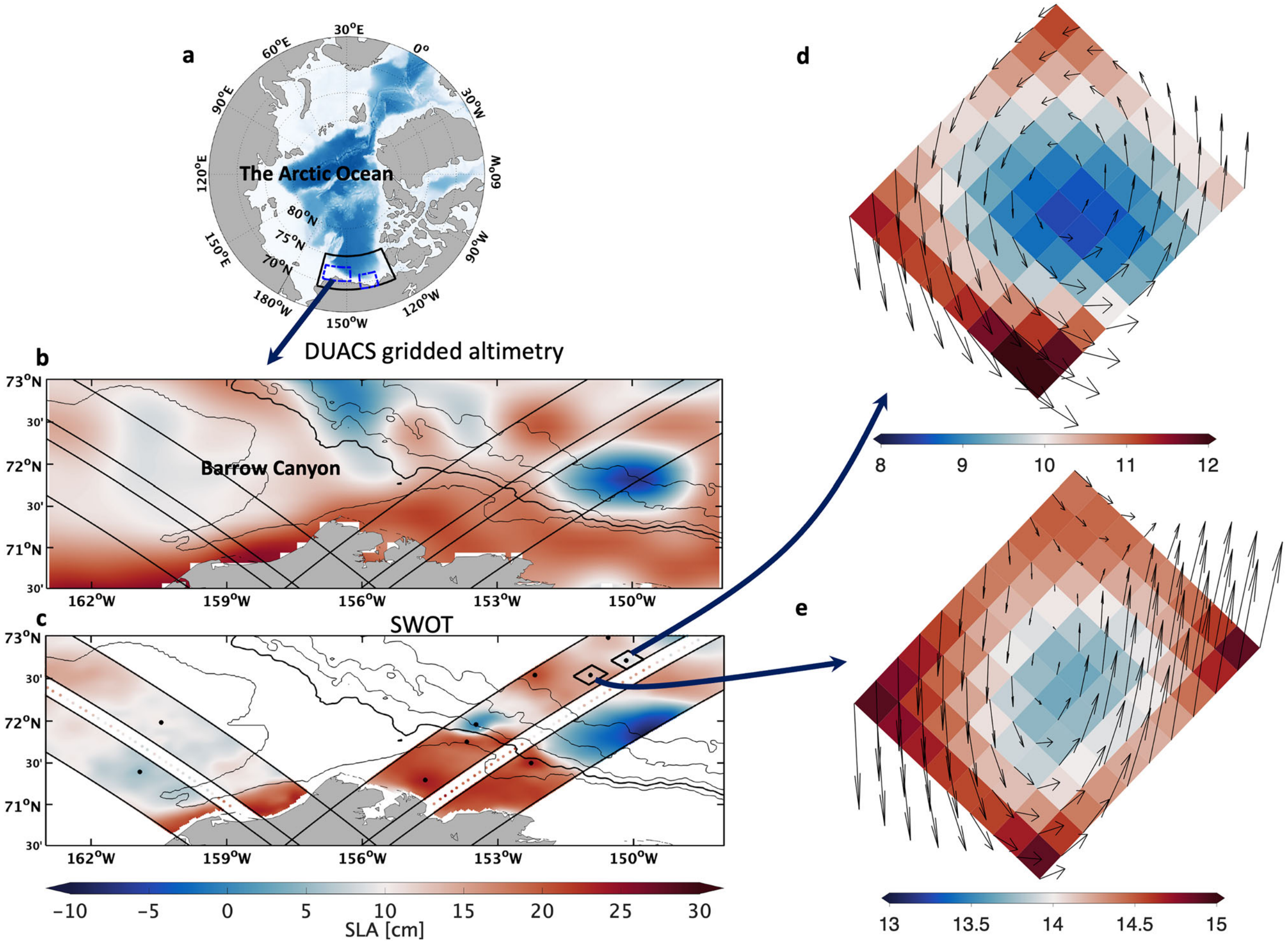

Fig. 1 | Unprecedented capability of SWOT to observe small Arctic eddies. a The Arctic Ocean bathymetry from ETOPO1 data, with the black box showing the Beaufort Sea and two blue dashed boxes denoting two subset regions; left: Barrow Canyon Region (BCR); right: Mackenzie River Region (MRR). **b** Snapshot of sea level anomalies (SLA) in BCR from 1/8° resolution CMEMS gridded satellite altimetry product on 14 September, 2024. The SWOT ground tracks corresponding to panel (**c**) are denoted for comparison. **c** Snapshots of SLA from two SWOT tracks passing over the BCR on 14 September 2024. The centers of eddies (black dots) detected by SWOT are depicted. Black contour lines represent the isobaths of 60, 300, 1000, 2000, and 3000 m, with the isobath of 300 m in bold. **(d, e)** Zoom-in views of the SLA fields for the two boxes in (**c**), showing eddy structures with superimposed geostrophic velocity anomaly vectors.

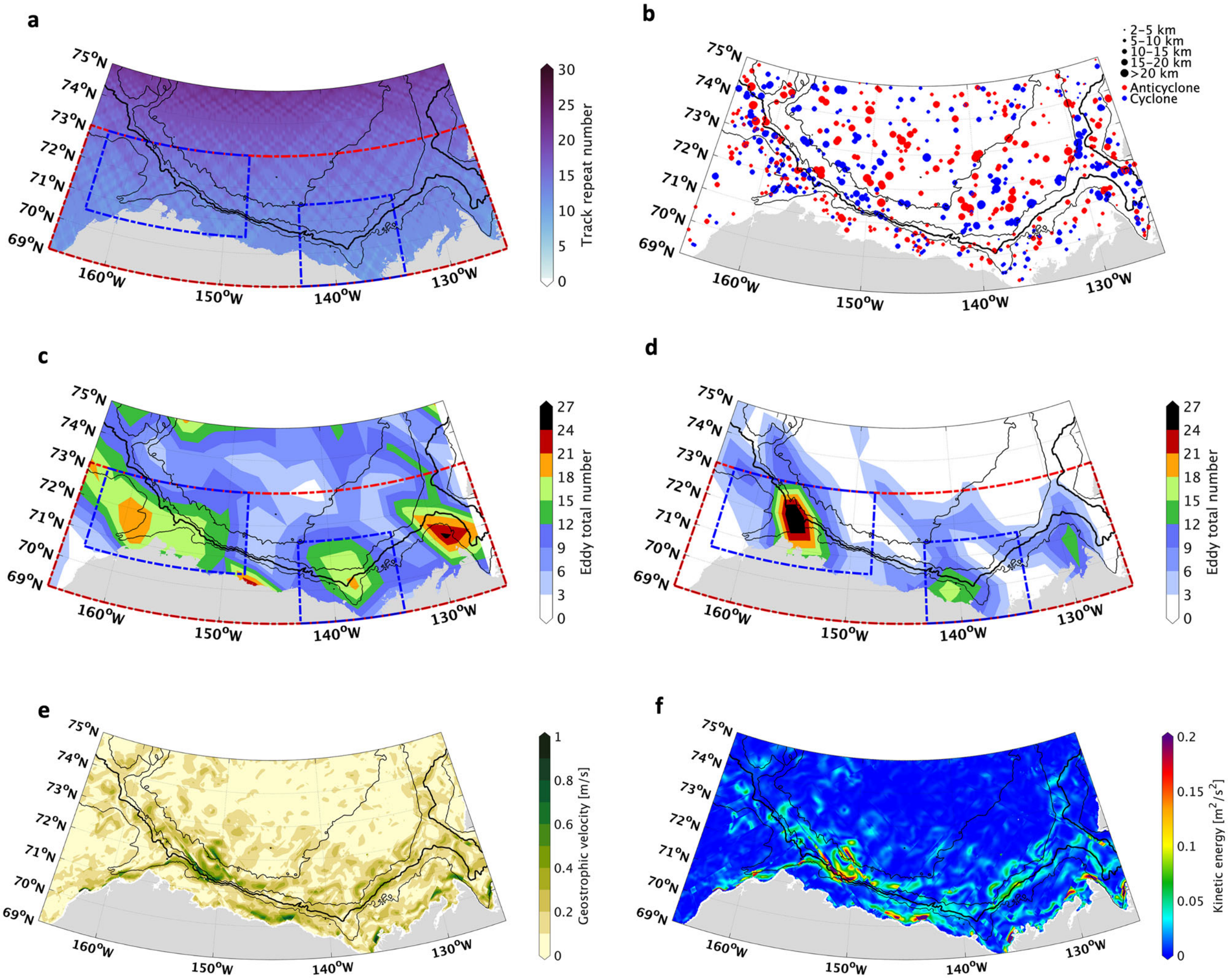

Fig. 2 | Three hotspots of eddies in the southern Beaufort Sea. a Number of SWOT sampling tracks in August 2024. **b** The location, size, and polarity of eddies identified from the SWOT sea level anomalies (SLA) in August 2024. **c** The total eddy number counted within 3° longitude x 1° latitude grid cells in August 2024 from SWOT. **d** The total eddy number counted within 3° longitude x 1° latitude grid cells in August 1998 from ARC60 (interpolated onto the SWOT tracks before analysis). The red dashed box denotes the southern Beaufort Sea, and the two blue dashed boxes indicate the BCR and MRR, respectively. **e** The composite snapshot of the geostrophic velocity anomaly magnitude derived from the SWOT SLA in August 2024. **f** The composite snapshot of the kinetic energy derived from the SWOT SLA in August 2024. Black contour lines represent the isobaths of 60, 300, 1000, and 3000 m, with the isobath of 300 m in bold.

both spatial density and temporal frequency of SLA observations compared to traditional altimeters. The geostrophic Rossby number (relative vorticity of the geostrophic flow normalized by the Coriolis parameter) is typically in the range −0.4 to 0.4 (Supplementary Fig. S1), suggesting that the inferred surface circulation remains in a regime where geostrophic dynamics are expected to be a good first-order approximation and cyclogeostrophic (centrifugal) corrections are secondary.

Hotspots of eddy activity associated with shelf-basin exchange

The SWOT observations reveal a distinct contrast in eddy characteristics between the continental shelf and interior basin in the Beaufort Sea (Fig. 2b). The continental shelf is populated with a higher density of small mesoscale eddies (radius of less than 10 km), while the interior basin hosts a mixture of small and slightly larger eddies. This pattern aligns with increased Rossby deformation radius offshore ($O(10km)$ in the interior basin versus $O(1km)$ over the shelf)[36]. Three major hotspots of eddy activity are identified in the southern Beaufort Sea (Fig. 2c and Supplementary Fig. S2a): (i) the Barrow Canyon Region (BCR), (ii) the Mackenzie River Region (MRR), and (iii) the entrance of the Amundsen Gulf. These regions exhibit increased eddy counts (>15 eddies per $3°\times1°$ bin per month). The persistence of these eddy hotspots is supported by consistent observations during other open-water months in 2023 and 2024 (Supplementary Fig. S3), as well as by comparisons with simulated eddy statistics from the ARC60 high-resolution ocean model for August 1998 (Fig. 2d). These findings indicate that Pacific Water intrusion and freshwater discharge from land serve as persistent drivers of eddy generation in these regions, through mechanisms of barotropic and baroclinic instability[37,38].

The SWOT observations exhibit enhanced geostrophic currents and higher kinetic energy in the southern Beaufort Sea than in the interior basin (Fig. 2e and f). These energetic features spatially coincide with the identified eddy hotspots (Fig. 2c). The detected coherent eddies near the coast of the southern Beaufort Sea also tend to have larger amplitudes and greater strength (Supplementary Fig. S2b and c).

The synergistic analysis of SWOT SLA observations with concurrent satellite measurements of Sea Surface Salinity (SSS), Sea Surface Temperature (SST) and Chlorophyll a concentration on August 6, 2024 reveals the critical role of mesoscale eddies in mediating freshwater, heat, and nutrient transport in the southern Beaufort Sea (Fig. 3 and Fig. 4). As an example, in the MRR, the river plume exhibits distinct signatures, with low-SSS (~ 24.5 PSU), high-SST (~ 11.5 °C), and Chlorophyll a-enriched (~ 5.5 mg/m^3) waters adjacent to the river mouth that gradually transition to more marine conditions offshore (Fig. 3). The SWOT observations along its two tracks on

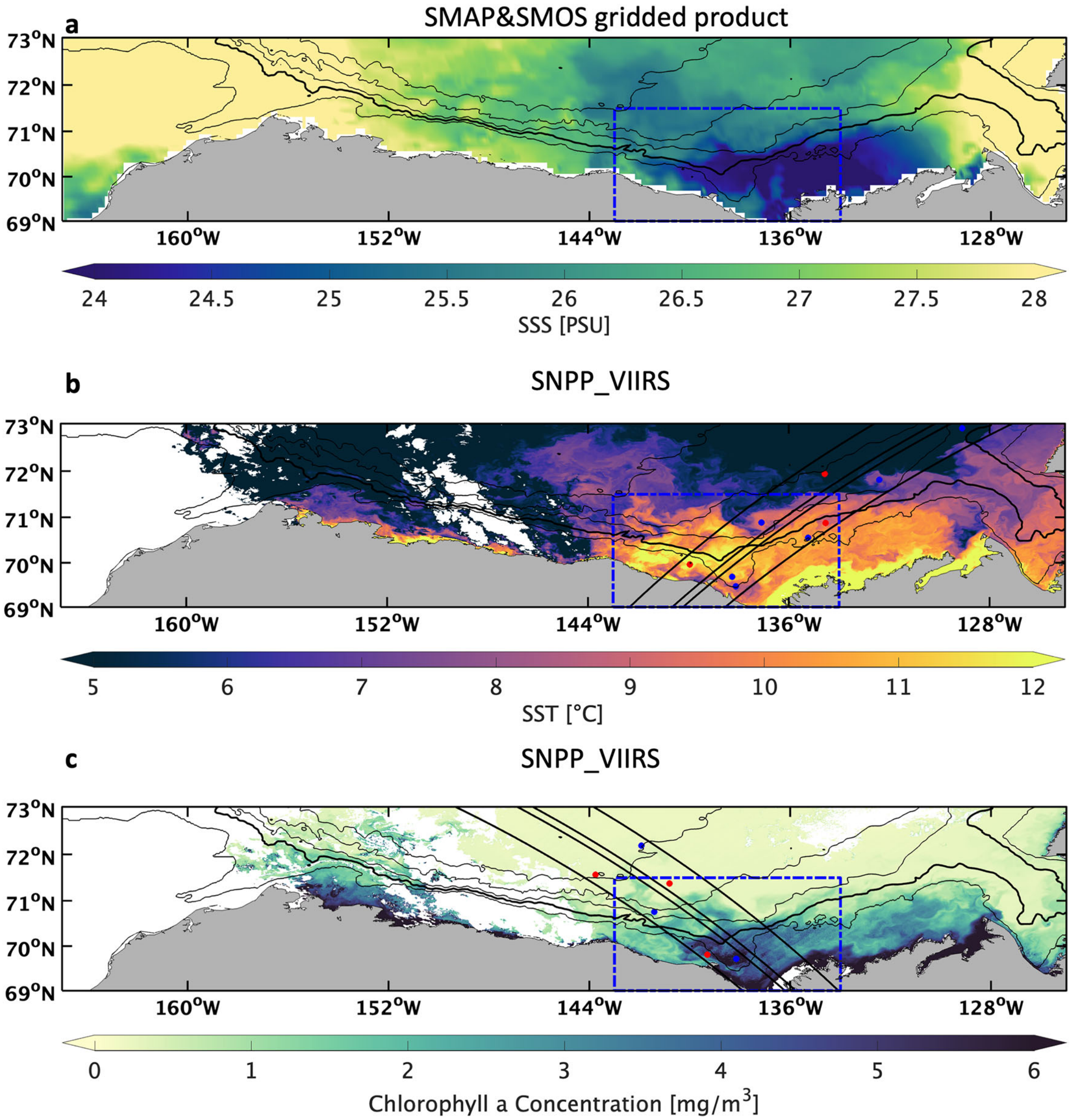

Fig. 3 | Eddy-modulated shelf-basin transports of freshwater, heat, and nutrients associated with the Mackenzie River plume. **a** Snapshot of sea surface salinity (SSS) from the 1/8° resolution gridded multi-observation product on August 6, 2024. **b**, **c** Snapshots of SNPP VIIRS 750 m resolution (**b**) sea surface temperature (SST) and (**c**) chlorophyll a concentration at 19:18 pm on August 6, 2024. The centers of the detected cyclones (blue dots) and anticyclones (red dots) are indicated in (**b**) and (**c**) over the SWOT track swaths (bounded by black lines). Black contour lines represent the isobaths of 60, 300, 1000, and 2000 m, with the isobath of 300 m in bold. The dashed blue boxes indicate the MRR.

this day reveal coherent eddies embedded in the spreading riverine waters (Fig. 3b and c).

The swirling and meandering structures associated with the offshore spreading of riverine waters demonstrate the active role of eddies in mediating offshore transport, as illustrated by the zoomed-in views in the MRR (Fig. 4a–d). Despite temporal offsets between the SWOT overpass and the SST/Chlorophyll a measurements on August 6, 2024, the mesoscale eddies detected by SWOT through distinct SLA signatures exhibit spatial coherence with patterns of both SST and Chlorophyll a concentration (Fig. 4a–d). Two of these eddies are highlighted in Fig. 4e and f, showcasing their characteristic SLA patterns and corresponding geostrophic current anomalies, with a radius (amplitude) of 7.7 km (−1.53 cm) for the cyclone (Fig. 4e) and 11.0 km (1.55 cm) for the anticyclone (Fig. 4f). The SWOT dataset enables a quantitative and systematic assessment of these small eddies, which have impacts on freshwater and heat budgets, as well as biogeochemistry in the interior Beaufort Sea.

Beyond the satellite-based evidence presented above, the role of small mesoscale eddies in facilitating shelf-basin exchange in the MRR is quantitatively confirmed by results from the ARC60 model (see Methods). The cumulative meridional heat and freshwater fluxes associated with eddy trapping during the summer of 1998 are directed northward, thereby enhancing offshore transport (Fig. 4g).

Eddy properties and statistics in the southern Beaufort Sea

Eddy characteristics in the southern Beaufort Sea during the summer months (August-October) of 2023 and 2024 are analyzed using SWOT observations. The total eddy count remains relatively stable (~400) throughout the study period, peaking in October 2023 (about 500) (Fig. 5a). Overall, cyclones outnumber anticyclones in each month. Differences are also evident in their properties (Fig. 5, b-e). On average, cyclones exhibit smaller radii, higher amplitudes, greater strength, and larger Rossby numbers compared to anticyclones (Fig. 5b–e). Averaged over the southern Beaufort Sea during the study period, the mean eddy

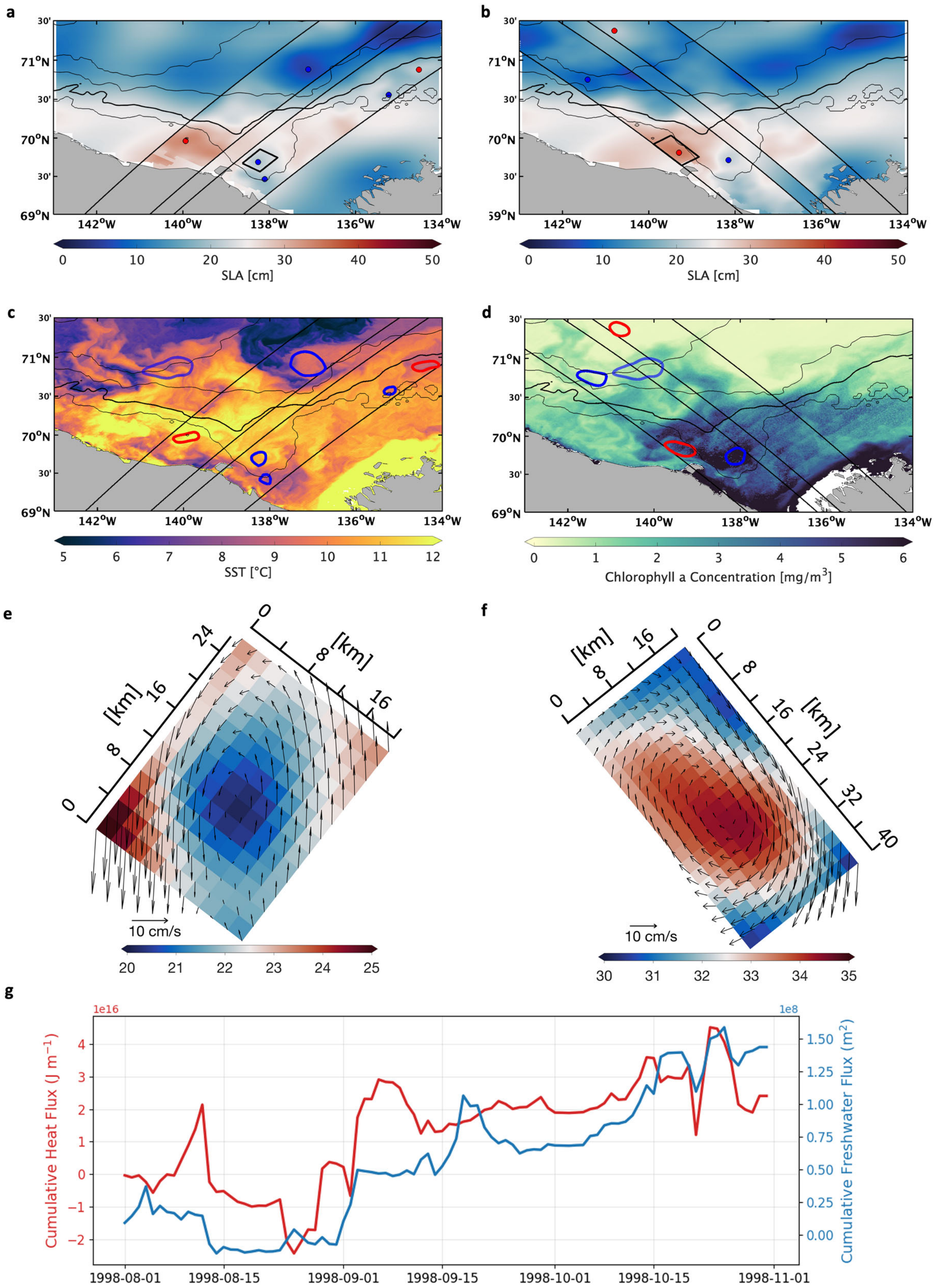

radius is 10.4 km, the mean eddy amplitude is 1.46 cm, the mean eddy strength is 10.1 cm/s, and the mean absolute Rossby number at eddy centers is 0.14.

Across the Beaufort Sea south of 75°N, the total eddy count exceeds 600 in each summer month (Supplementary Fig. S4). The maximum eddy count is also observed in October 2023, followed by August in both 2023 and 2024 (Supplementary Fig. S4). The mean eddy amplitude and strength are generally higher in the BCR than in other areas, with amplitudes exceeding 1.5 cm and strengths surpassing 10 cm/s in all the summer months (Supplementary Fig. S5). In the MRR, the mean eddy amplitude and strength are slightly higher than the average over the Beaufort Sea (Supplementary Fig. S6).

Fig. 4 | Small mesoscale eddies associated with river plumes detected by SWOT. **a**, **b** 2 km resolution filtered sea level anomalies (SLA) from SWOT pass #5 **a** and pass #13 **b** on August 6, 2024, overlaid over the 1/8° resolution gridded altimetry SLA from August 6, 2024. The centers of the detected cyclones (blue dots) and anticyclones (red dots) on the SWOT swaths are indicated. Zoom-in (**c**) sea surface temperature (SST) and (**d**) chlorophylla concentration for the Mackenzie River Region (MRR; blue box in Fig. 3). The edges of the detected cyclones (blue contours) and anticyclones (red contours) on the SWOT swaths are shown. One cyclone that was detected the next day, on August 7, 2024, is also shown with a blue contour with 0.6 transparency. Black contour lines represent the isobaths of 60, 300, 1000, and 2000 m, with the isobath of 300 m in bold. Zoom-in view of the SLA fields for (**e**) a cyclone (location indicated in (**a**)) and (**f**) an anticyclone (location indicated in (**b**)), showing the eddy structure with superimposed geostrophic velocity anomaly vectors observed by SWOT. **g** Time series of cumulative meridional heat and freshwater fluxes associated with eddy trapping in the MRR during three months of 1998 simulated by the ARC60 model. Only small eddies with a radius smaller than 15 km are taken into account. An increase with time indicates northward transport.

Although SWOT provides frequent coverage of the Beaufort Sea, the daily sampling remains spatially limited. To assess whether the SWOT-detected eddies are representative of the overall regional eddy properties, we compared SWOT-derived eddy number and properties (polarity, radius, amplitude, and strength) with those extracted from ARC60 model output. The model data are interpolated onto the SWOT track swaths and onto a regular grid covering the southern Beaufort Sea. This dual interpolation approach allows us to assess potential sampling biases in SWOT and model biases in ARC60.

During the summer months (August-October) in 2023 and 2024, SWOT observations reveal a slightly asymmetric distribution of cyclones and anticyclones, with a weak bias toward cyclones in terms of eddy count (55.1% versus 44.9%). Cyclones exhibit marginally smaller radii, higher amplitudes, and stronger strength compared to anticyclones (Fig. 6). The observed eddies are predominantly characterized by radii of 5–15 km, absolute amplitude of 0.5–2 cm, and strength of 5–15 cm/s. When the ARC60 output is sampled along the same SWOT track swaths for the summer months of 1997 and 1998, the model has a substantially lower count of detected eddies, with a much stronger bias toward cyclones (70.7% versus 29.3%; Fig. 6a). The model indicates a systematic eddy size overestimation (Fig. 6b), a shift to higher eddy amplitudes (Fig. 6c), and a slight skew toward weaker eddies (Fig. 6d). Our results underscore limitations in the high-resolution model's representation of eddy abundance, polarity, size, and, to some extent, amplitude, addressing the value of SWOT for evaluating and improving high-resolution models.

When interpolating daily model output onto a nominal 0.03° longitude × 0.01° latitude grid covering the entire southern Beaufort Sea, the model bias toward cyclones persists (76.2% versus 23.8%; Fig. 6a). The radius and strength distributions become slightly more skewed between cyclones and anticyclones (Fig. 6b and d). Although most eddies are smaller than 15 km, a notable portion have radii larger than 25 km, particularly for the anticyclones (Fig. 6b). These large mesoscale eddies are missed in the SWOT tracks due to the 50 km swath width limitation. This contributes to the difference between the two versions of eddy strength in model results (Fig. 6d). While excluding eddies with radii larger than 25 km (Fig. 6e), the SWOT-track-sampled and fully-gridded model data show more similar distributions (Fig. 6e). These findings indicate that, despite its sampling limitation in spatial coverage, SWOT observations effectively capture the key statistical properties of mesoscale eddies in the region, except for those larger than the swath width.

The characteristics of eddies derived from the 1/8°-resolution gridded altimetry product (provided by Copernicus Marine Environment and Monitoring Service; CMEMS) and from the gridded altimetry product incorporating SWOT data (Multiscale Inversion of Ocean Science Topography; MIOST) are further analyzed (Supplementary Fig. S7). In the southern Beaufort Sea, eddies identified from these gridded products exhibit a nearly equal partitioning between cyclones and anticyclones, consistent with previous analyses[13]. Most eddies have radii larger than 15 km, substantially larger than those detected by SWOT. They also exhibit larger absolute amplitudes but weaker strength. These gridded altimetry products are unable to resolve small mesoscale eddies in the Arctic Ocean. As shown above, the SWOT dataset enables the first quantitative and systematic assessment of these small eddies.

Discussion and summary

This study investigates the spatial and temporal variability of surface mesoscale features in the Beaufort Sea by utilizing the recent high-resolution SWOT satellite observations. This technological advancement enables the direct observation of small Arctic mesoscale eddies that were previously undetectable with conventional satellite altimetry products (Fig. 1). Our findings highlight the revolutionary potential of SWOT to advance the understanding of Arctic mesoscale processes. By combining the SWOT data with other satellite observations and a km-scale ocean model, our study identifies key hotspots of eddy generation and reveals their roles in transporting nutrient-rich freshwater from the shelf across the continental slope of the Beaufort Sea. The unprecedented SWOT resolution allows for robust estimates of eddy characteristics and statistics during the summer months, providing valuable insights for ocean model development and evaluation.

The SWOT observations reveal three hotspots of mesoscale eddies in the southern Beaufort Sea, in contrast with lower eddy activity observed in the interior of the Beaufort Gyre (Fig. 2). Eddy generation in the BCR is driven by both barotropic instability introduced through horizontal current shear[38] and baroclinic instability arising from density gradients[37,39]. These processes are closely linked to the wind-modulated Pacific Water inflow through the Barrow Canyon[40–42]. In the MRR, warm and fresh Mackenzie River Water interacts with colder and saltier Arctic Water, creating drastic density gradients that set an unstable background state favorable to baroclinic instability[43]. The upper circulation at the mouth of Amundsen Gulf is predominantly wind-driven, and the presence of distinct water masses forms frontal structures and catalyzes eddy generation[44,45].

The observed coherence between eddy signatures from SWOT and surface anomalies in SST and Chlorophyll a concentration suggests the importance of mesoscale eddies in shelf-basin exchange in the southern Beaufort Sea (Figs. 3 and 4). Results from the ARC60 model further support this interpretation, showing that small mesoscale eddies trap and transport heat and freshwater northward in the MRR during the summer months. By modulating shelf-basin exchange, eddies could provide a shorter and more efficient route for the poleward transport of heat, freshwater, and biogeochemical tracers. This process has strong implications for freshwater content, upper-ocean stratification, sea ice cover, and biogeochemistry in the interior Beaufort Sea[14–17].

For eddies with radii observable by SWOT (2–25 km), our analysis indicates a mean radius of about 10 km (Fig. 5), with a substantial fraction smaller than this average (Fig. 6b). This addresses the necessity of the high spatial resolution offered by SWOT for characterizing eddies in the Arctic. Our analysis reveals a weak polarity bias toward cyclones in the southern Beaufort Sea (Fig. 6a). This finding helps reconcile discrepancies among different studies, including the reported anticyclone dominance from ITP in-situ measurements[19,20,46], the cyclone dominance identified in SAR imagery[12], and the strong cyclone bias in the high-resolution model ARC60. The eddy characteristics and statistics, based on the SWOT analysis presented in this study, establish a fundamental basis for informing future high-resolution ocean development and evaluation. Eddy properties derived from ARC60, sampled along SWOT tracks and across the entire domain on a regular grid, are broadly consistent for small mesoscale eddies (Fig. 6). This confirms that SWOT's capability to provide basin-scale eddy statistics remains robust despite its intermittent orbital sampling.

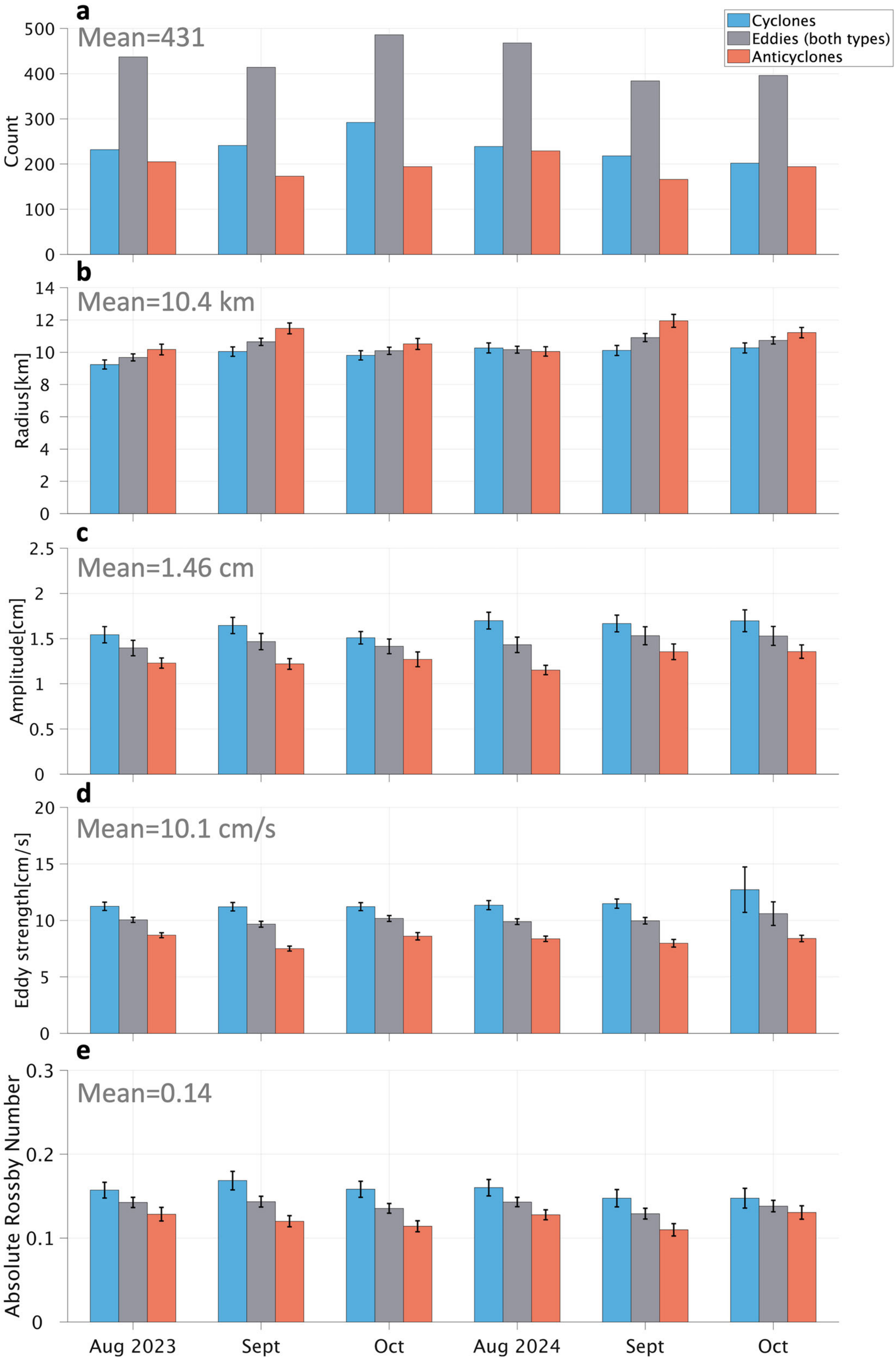

Fig. 5 | Eddy characteristics in the southern Beaufort Sea revealed by SWOT. **a** Eddy count. **b** Eddy radius. **c** Eddy absolute amplitude. **d** Eddy strength. **e** Absolute Rossby number at the centers of eddies. Results for cyclonic eddies, anticyclonic eddies, and both types of eddies are shown with blue, red, and grey colors, respectively. The mean values for eddy count and properties averaged over all available summer months are denoted in each panel. The error bars in (**b**–**e**) represent the standard error of the monthly mean. Note that the SWOT data during September 22–26, 2023, are missing.

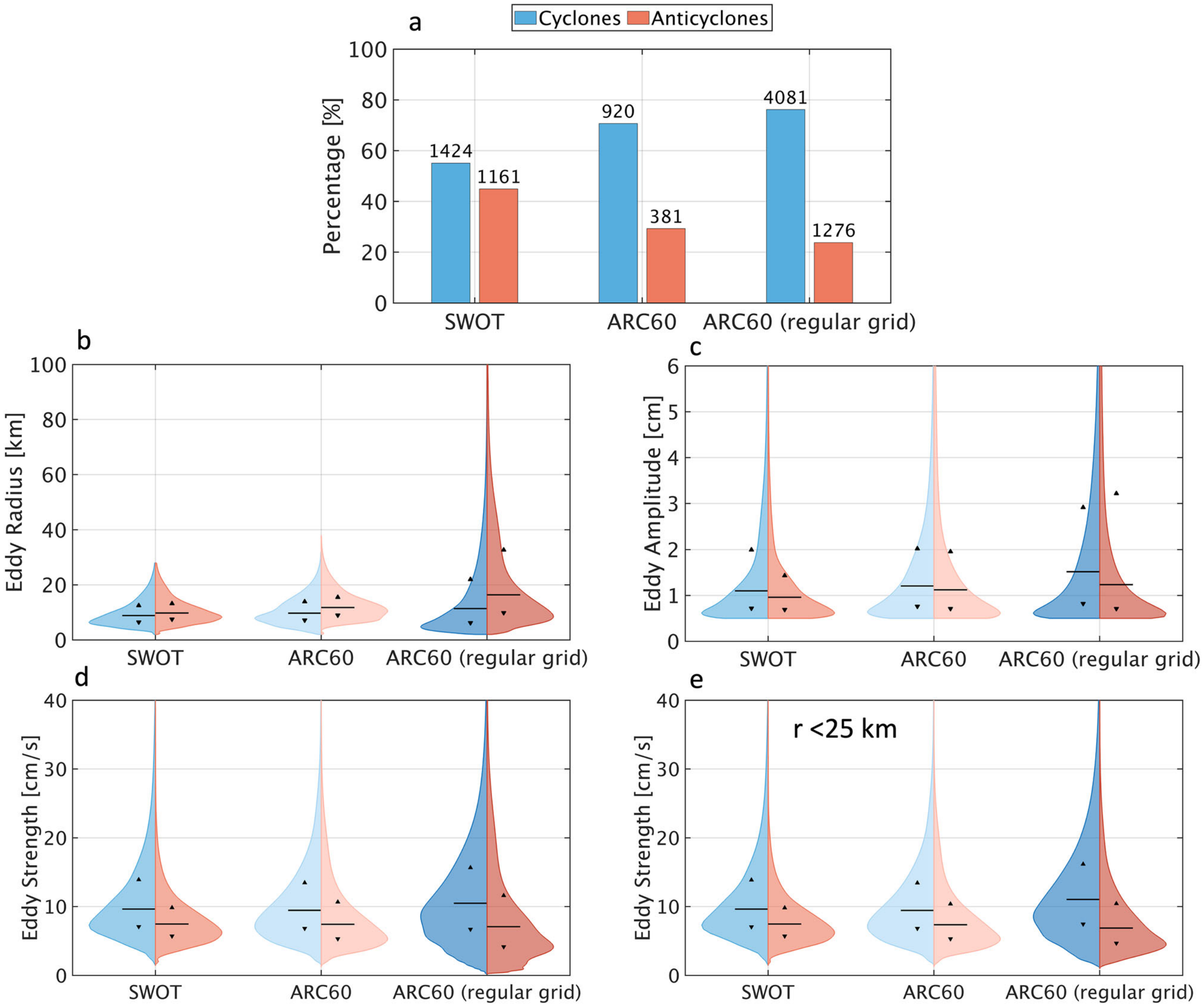

Fig. 6 | Statistics of eddies in the southern Beaufort Sea from SWOT observations and ARC60 model results. a Eddy polarity percentage and eddy count. **b** Eddy radius. **c** Eddy absolute amplitude. **d** Eddy strength. **e** Eddy strength for the eddies with radii smaller than 25 km. Eddies detected over the summer months of 2023 and 2024 from SWOT (1997 and 1998 from ARC60) are all considered. ARC60 SLA in 1997 (1998) is interpolated onto the SWOT track swaths in 2023 (2024). ARC60 (regular grid) represents the case in which the model SLA is interpolated onto a regular 0.03° longitude x 0.01° latitude grid. The distributions for cyclones are shown in blue, and anticyclones in red. The solid middle lines in the violin plots indicate the median, while the upward- and downward-pointing triangles mark the 75th and 25th quantiles, respectively.

Despite its transformative capabilities, SWOT has certain limitations. The long repeat cycle of the SWOT orbital tracks means that we cannot track the evolution of eddies, making it difficult to obtain eddy trajectories, translational speeds, and their lifetimes. Additionally, the SWOT swath width excludes the detection of eddies with radii larger than 25 km. Future research should leverage longer time series of SWOT observations and explore synergies with other satellite missions, hydrographic measurements, and high-resolution ocean modelling to deepen our understanding of eddy dynamics and their climatic and biogeochemical implications in the high-latitude oceans. Compared with SWOT observations, the high-resolution ocean model tends to simulate fewer and larger eddies with an amplified asymmetry in polarity. Besides inherent model biases, differences in the years considered may also contribute to these discrepancies.

Methods

SWOT data

After 20 years of preparation, planning, and development, the SWOT satellite mission was successfully launched in December 2022. This dataset allows the observation of finer-scale ocean surface structures and provides a critical benchmark in understanding ocean dynamics. We leverage the latest SWOT_L3_LR_SSH ['Expert'] product version 3.0, which is derived from the L2 SWOT Ka-band Radar Interferometer (KaRIn) low rate ocean data products provided by NASA/JPL and CNES, with participation of the Canadian and British space agencies. This dataset is produced and made freely available by the AVISO and DUACS teams as part of the DESMOS Science Team project[47]. The L3 product has been cross-calibrated with the DUACS SLA dataset to enable direct comparison and demonstrates clear improvements in resolution and accuracy.

The SWOT measurements along a Nadir altimeter track include two 50-km-wide KaRIn 2D swaths with a gap of 20 km in between. We have chosen the filtered Sea Level Anomaly (SLA) field for our analysis, which has undergone corrections, calibration, and noise reduction. The spatial resolution of the SWOT SLA measurements is 2 km[33]. The denoising and filtering algorithm applies a convolutional neural network (CNN) that is based on a U-Net architecture and is retrained with the NEMO-eNATL60 ocean model with tides[48]. The retraining is conducted using random-wave-modulated white noise at 250 m resolution, followed by the application of a Hamming filter to replicate the 2 km downscaling performed in the ground processing segment. The detailed processing methodology is described in Tréboutte et al. [49] and Dibarboure et al. [48]. The instrument noise in SWOT data has been reduced by approximately an order of magnitude compared to traditional radar altimetry and was found to be less than 0.4 cm[33,50]. To ensure statistical robustness, only eddies with absolute amplitude greater than 0.5 cm are included in our analysis. The SLA field used is referenced to a beta version of the mean sea surface (MSS) CNES_CLS_2025[51]. The MSS error along the SWOT KaRIn tracks accounts for only 2.7% of the estimated SLA variance at wavelengths between 10 and 100 km. This represents a significantly improved level of accuracy compared to the previous hybrid MSS product[52,53]. The temporal evolution of the detected eddies suggests that noise in the MSS has a minor impact on eddy identification (Supplementary Fig. S3).

The SWOT mission has a nominal operational lifetime of 42 months, comprising three sequential phases: a 3-month engineering checkout period, a 3-month calibration and validation phase from March 29 to July 11, 2023, and a minimum planned 36-month science phase for global mapping operation starting from July 26, 2023[33]. In the Beaufort Sea, the SLA field with sea ice concentration above 30% is masked. We utilize the SWOT's 21-day cycle data from the science phase and reorganize them by month for 2023 and 2024, enabling us to better quantify the temporal variability in the eddy statistics. We conduct our analysis during the three summer months (August, September, and October) for these two years when the Beaufort Sea is completely sea ice-free to exclude the influence of sea ice on the observations.

Gridded altimetry and SSS data

The gridded satellite altimetry data for SLA and Sea Surface Salinity (SSS) are freely made available by the Copernicus Marine Environment and Monitoring Service (CMEMS; http://marine.copernicus.eu/). The SLA product is processed by the DUACS multimission altimeter data processing system[31] (http://duacs.cls.fr) that is developed by CNES/CLS (product ID: SEALEVEL_GLO_PHY_L4_MY_008_047). The SLA is estimated using Optimal Interpolation (OI), which combines L3 along-track measurements from multiple available altimeter missions, ranging from GEOSAT to Jason-3, and serves in delayed-time applications. The data are provided daily on a 1/8° regular grid, which provides ~14 km horizontal resolution in the Beaufort Sea. The SSS product provides Near-Real-Time (NRT) daily data at 1/8° resolution, which is obtained through a multi-dimensional (multivariate) OI algorithm that combines SSS images from multiple satellite sources including NASA's Soil Moisture Active Passive (SMAP) and ESA's Soil Moisture Ocean Salinity (SMOS) satellites with in-situ salinity measurements and satellite SST information (product ID: MULTIOBS_GLO_PHY_S_SURFACE_MYNRT_015_013). The product was developed by the CNR[54,55]. The global Multiscale Inversion of Ocean Science Topography (MIOST) gridded altimetry product (L4) integrates nadir along-track data from CMEMS and wide-swath SWOT L3 v2.0.1 data, combining them using mapping techniques, including multiscale and multivariate interpolation and data-driven interpolation approaches[56,57].

VIIRS SST and ocean color data

The Sea Surface Temperature (SST) and Chlorophyll a concentration are derived from the Suomi National Polar-orbiting Partnership (NPP) Visible Infrared Imaging Radiometer Suite (VIIRS) satellite. The VIIRS builds upon and extends the measurements collected by its predecessors, such as NASA's MODIS and NOAA's AVHRR[58]. It captures global satellite observations spanning the visible and infrared wavelengths over land, ocean, and atmosphere, including nighttime lights. We utilize the NRT L2 VIIRS dataset at a 750 m resolution, which is available from the NASA Ocean Color archives (https://oceancolor.gsfc.nasa.gov/). Although the VIIRS observations are sparse in the Beaufort Sea, they have undergone standard atmospheric correction to account for atmospheric and sea surface effects. They are thus less susceptible to common artifacts, including sun glint, thin clouds, stray light, and sensor saturation, and are well-suited to identify mesoscale eddy surface signatures[59,60].

High-resolution numerical model setup

We use the coupled ocean-sea ice model Nucleus for European Modelling of the Ocean (NEMO version 3.6; https://www.nemo-ocean.eu). NEMO includes Océan PArallélisé (OPA) engine for ocean dynamics and thermodynamics, and Louvain-la-neuve Ice Model (LIM) module for sea-ice dynamics and thermodynamics[61–63]. Based on the NEMO framework, ARC60 is a pan-Arctic configuration that covers the whole Arctic Ocean with an extremely high mesoscale eddy-resolving resolution of 1/60°, extracted from the corresponding tripolar ORCA grids. This is a 1/60° configuration with 50 vertical levels. In the Beaufort Sea, the horizontal resolution is about 800 m. The initial conditions, including 3D ocean fields (temperature, salinity, zonal and meridional velocities) as well as 2D SLA and sea ice fields (concentration and thickness), are obtained from the GLobal Ocean ReanalYsis and Simulations 2 version 4 (GLORYS2v4) produced by Mercator Ocean[64]. Monthly open boundary conditions (temperature, salinity, and horizontal ocean velocities) are also derived from the GLORYS2v4 dataset. The atmospheric forcing (10 m wind, 2 m air temperature, specific humidity, precipitation minus evaporation, and radiation fluxes) is obtained from the ERA5 reanalysis product, which has high spatial and temporal resolution[65]. ARC60 features tides[66] and embeds both liquid runoff and solid ice discharge from Greenland[67–69]. The background vertical diffusivity is 10^{-5} m^2/s, and vertical viscosity is 10^{-4} m^2/s. The turbulent kinetic energy (TKE) scheme is applied to represent vertical mixing[70]. ARC60 is still running, and we now have an integration for the first seven years, from 1993 to 1999, at the time of writing this paper. Model outputs for 1997 and 1998 are used for our purpose to understand the representativeness of eddies observed along the SWOT tracks for the overall eddy properties in the study region.

Eddy detection scheme

Our analysis focuses on eddies with clearly identifiable surface signatures. Eddies are detected from 2-km SWOT track swaths, gridded altimetry products, and ARC60 model output using a widely adopted contour-based method applied to the SLA field[71]. The closed contours were scanned from the SLA field with an interval of 0.1 cm. The eddy center is defined as the average position of the innermost closed contour, while the eddy edge corresponds to the outermost closed contours that enclose no more than one eddy center. The eddy radius is computed as the radius of a perfect circle that has the same area as the detected eddy, and the eddy amplitude is calculated as the SLA difference between the eddy center and the eddy edge. A cyclone has a negative amplitude, whereas an anticyclone has a positive amplitude with an elevated surface height in the center. Since most of the detected eddies in the Beaufort Sea are mesoscale eddies and thus in approximately geostrophic balance (Supplementary Fig. S1), the eddy strength is defined as $V = \left|\frac{g}{f}\frac{\Delta\eta}{\Delta r}\right|$ where g is the gravitational acceleration, f is the Coriolis parameter, $\Delta\eta$ denotes the eddy amplitude, and Δr is the eddy radius. Considering the SWOT accuracy, eddies with the absolute values of amplitudes smaller than 0.5 cm are neglected.

To determine how circular an eddy is, we compute the eddy roundness as $R = \frac{4\pi A}{P^2}$ where A is the area enclosed by the eddy edge, P is the perimeter of the eddy. The results show that more than 90% of the detected eddies with absolute amplitude larger than 0.5 cm in the Beaufort Sea are coherent eddies with roundness larger than 0.6 (Supplementary Fig. S8). Since the vast majority of detected eddies are both strong and coherent, it suggests that the signals from internal waves, which are difficult to be distinguished from eddies[72], do not have a strong influence on the detection of small mesoscale eddies.

Rossby number

In a two-dimensional horizontal oceanic flow, the relative vorticity arising from ocean circulation is defined as $\zeta = \frac{\partial v}{\partial x} - \frac{\partial u}{\partial y}$, where u and v represent the zonal and meridional SWOT-derived surface geostrophic velocity, respectively. A positive value ζ indicates a cyclonic circulation, while a negative value signifies an anticyclonic circulation. The planetary vorticity, also known as the Coriolis parameter f, results from Earth's rotation and is given by $f = 2\Omega \sin\varphi$, where $\Omega = 7.292\times10^{-5}$ rad/s is the angular velocity of Earth's rotation, and φ is the latitude. The Rossby number is the relative vorticity normalized by the Coriolis parameter $Ro = \frac{\zeta}{f}$, which we use to illustrate eddy polarity and determine whether the eddies are mesoscale ($Ro{\sim}O(0.1)$) or submesoscale ($Ro{\sim}O(1)$)[73].

Heat and freshwater fluxes of eddies

To illustrate the role of eddies in shelf-basin exchange, we estimate the meridional surface heat and freshwater transport induced by eddy trapping by combining eddy translational velocity, eddy size, and the mean SST and SSS anomalies within each eddy. Integrated meridional heat and freshwater fluxes carried by eddies are computed as follows[74]:

$$F_H = v\cdot(2R)\cdot\rho_o\cdot c_p\overline{SST'} \quad (1)$$

$$F_{FW} = v\cdot(2R)\cdot\overline{\left(\frac{S_{ref}-SSS}{S_{ref}}\right)'} \quad (2)$$

Where v is the meridional translational velocity of an individual eddy, R is the radius of the eddy, $\rho_o = 1025kgm^{-3}$ is the mean seawater density, and $c_p = 4200J\ kg^{-1}\ K^{-1}$) is the average specific heat capacity for seawater.

The daily SST anomaly at the grid point is defined relative to the mean state of the SST during summer months (August-October) in 1998 at the respective grid point, and the eddy-mean anomaly is calculated by averaging within the eddy boundary. Freshwater $\left(FW = \frac{S_{ref}-SSS}{S_{ref}}\right)$ is defined with respect to a reference salinity $S_{ref} = 34.8$, which represents the Arctic mean salinity. The freshwater anomaly associated with each eddy is calculated in a manner similar to the SST anomaly. Cumulative fluxes are obtained by integrating the daily meridional fluxes over the summer months and across the MRR. An increase in their values indicates northward transport of heat or freshwater. Because our objective is mainly to demonstrate that the observed small eddies can facilitate offshore transport of heat and freshwater, we focus here on the transport associated with eddy trapping. The contribution of eddy stirring due to eddy rotation motion[75,76], which also drives offshore heat and freshwater transport across meridional temperature and salinity gradients, is not considered in this study.

Data availability

All data used in this study are publicly accessible. The SWOT Level-3 KaRIn SSH data are available from the AVISO repository (https://doi.org/10.24400/527896/A01-2023.018). The gridded satellite data can be downloaded from (https://doi.org/10.48670/moi-00148) for SLA and (https://doi.org/10.48670/moi-00051) for SSS. The MOIST Level-4 SSH data can be accessed through (https://doi.org/10.24400/527896/a01-2025.001). The VIIRS SST and ocean color data are available at (https://oceandata.sci.gsfc.nasa.gov/directdataaccess/Level-2/SNPP-VIIRS/). The ARC60 simulation source code can be accessed from (https://doi.org/10.5683/SP3/D4A9CL).

Code availability

The data analysis and plotting were performed using MATLAB R2018b. Codes that were created in this study are available from the corresponding author or the first author upon reasonable request.

Received: 23 September 2025; Accepted: 31 March 2026;
Published online: 13 April 2026

References

1. Giles, K. A., Laxon, S. W., Ridout, A. L., Wingham, D. J. & Bacon, S. Western Arctic Ocean freshwater storage increased by wind-driven spin-up of the Beaufort Gyre. *Nat. Geosci.* **5**, 194–197 (2012).
2. Morison, J. et al. Changing Arctic Ocean freshwater pathways. *Nature* **481**, 66–70 (2012).
3. Kelly, S. J., Proshutinsky, A., Popova, E. K., Aksenov, Y. K. & Yool, A. On the origin of water masses in the Beaufort Gyre. *J. Geophys. Res. Oceans* **124**, 4696–4709 (2019).
4. Proshutinsky, A. et al. Analysis of the Beaufort Gyre freshwater content in 2003–2018. *J. Geophys. Res.: Oceans* **124**, 9658–9689 (2019).
5. Wang, Q. et al. Arctic Sea ice decline significantly contributed to the unprecedented liquid freshwater accumulation in the Beaufort Gyre of the Arctic Ocean. *Geophys. Res. Lett.* **45**, 4956–4964 (2018).
6. Zhang, J. et al. Labrador Sea freshening linked to Beaufort Gyre freshwater release. *Nat. Commun.* **12**, 1229 (2021).
7. Logerwell, E. et al. Fish communities across a spectrum of habitats in the western Beaufort Sea and Chukchi Sea. *Prog. Oceanogr.* **136**, 115–132 (2015).
8. Jarvela, L. E. & Thorsteinson, L. K. The epipelagic fish community of Beaufort Sea coastal waters, Alaska. *Arctic* **52**, (1999).
9. Zhao, M. & Timmermans, M. Vertical scales and dynamics of eddies in the Arctic Ocean's Canada Basin. *JGR Oceans* **120**, 8195–8209 (2015).
10. D'Asaro, E. A. Observations of small eddies in the Beaufort Sea. *J. Geophys. Res.* **93**, 6669–6684 (1988).
11. Muench, R. D., Gunn, J. T., Whitledge, T. E., Schlosser, P. & Smethie, W. An Arctic Ocean cold core eddy. *J. Geophys. Res.* **105**, 23997–24006 (2000).
12. Kozlov, I. E., Artamonova, A. V., Manucharyan, G. E. & Kubryakov, A. A. Eddies in the Western Arctic Ocean from Spaceborne SAR observations over open ocean and marginal ice zones. *JGR Oceans* **124**, 6601–6616 (2019).
13. Kubryakov, A. A., Kozlov, I. E. & Manucharyan, G. E. Large mesoscale eddies in the western Arctic Ocean from satellite altimetry measurements. *J. Geophys. Res.: Oceans* **126**, 1–26 (2021).
14. Armitage, T. W. K. K., Manucharyan, G. E., Petty, A. A., Kwok, R. & Thompson, A. F. Enhanced eddy activity in the Beaufort Gyre in response to sea ice loss. *Nat. Commun.* **11**, (2020).
15. Manucharyan, G. E. & Spall, M. A. Wind-driven freshwater buildup and release in the Beaufort Gyre constrained by mesoscale eddies. *Geophys. Res. Lett.* **43**, 273–282 (2016).
16. Watanabe, E., Kishi, M. J., Ishida, A. & Aita, M. N. Western Arctic primary productivity regulated by shelf-break warm eddies. *J. Oceanogr.* **68**, 703–718 (2012).
17. Watanabe, E. et al. Enhanced role of eddies in the Arctic marine biological pump. *Nat. Commun.* **5**, (2014).
18. Manucharyan, G. E. & Thompson, A. F. Heavy footprints of upper-ocean eddies on weakened Arctic sea ice in marginal ice zones. *Nat. Commun.* **13**, 2147 (2022).
19. Zhao, M. et al. Characterizing the eddy field in the Arctic Ocean halocline. *J. Geophys. Res. Oceans* **119**, 8800–8817 (2014).
20. Zhao, M., Timmermans, M.-L., Cole, S., Krishfield, R. & Toole, J. Evolution of the eddy field in the Arctic Ocean's Canada Basin, 2005–2015. *Geophys. Res. Lett.* **43**, 8106–8114 (2016).
21. Auger, M., Sallée, J., Thompson, A. F., Pauthenet, E. & Prandi, P. Southern ocean ice-covered Eddy properties from satellite altimetry. *JGR Oceans* **128**, (2023).
22. Chelton, D. B., Schlax, M. G. & Samelson, R. M. Global observations of nonlinear mesoscale eddies. *Prog. Oceanogr.* **91**, 167–216 (2011).
23. Fu, C., Müller, V. & Myers, P. G. Large mesoscale Eddy properties and dynamics in the Labrador sea from satellite altimetry. *Atmos. Ocean* 1–19 (2025).
24. Regan, H., Lique, C., Talandier, C. & Meneghello, G. Response of Total and Eddy Kinetic Energy to the Recent Spinup of the Beaufort Gyre. *J. Phys. Oceanogr.* **50**, 575–594 (2020).
25. Meneghello, G. et al. Genesis and decay of mesoscale baroclinic eddies in the seasonally ice-covered interior Arctic Ocean. *J. Phys. Oceanogr.* **51**, 115–129 (2021).

26. Wang, Q. et al. Eddy kinetic energy in the Arctic Ocean from a global simulation with a 1-km Arctic. *Geophys. Res. Lett.* **47**, e2020GL088550 (2020).
27. Hattermann, T. et al. Eddy-driven recirculation of Atlantic Water in Fram Strait. *Geophys. Res. Lett.* **43**, 1–9 (2016).
28. Wekerle, C. et al. Properties and dynamics of mesoscale eddies in Fram Strait from a comparison between two high-resolution ocean–sea ice models. *Ocean Sci.* **16**, 1225–1246 (2020).
29. Zhang, Z. et al. Submesoscale eddies detected by SWOT and Moored Observations in the Northwestern Pacific. *Geophys. Res. Lett.* **51**, e2024GL110000 (2024).
30. Archer, M., Wang, J., Klein, P., Dibarboure, G. & Fu, L.-L. Wide-swath satellite altimetry unveils global submesoscale ocean dynamics. *Nature* **640**, 691–696 (2025).
31. Taburet, G. et al. DUACS DT2018: 25 years of reprocessed sea level altimetry products. *Ocean Sci.* **15**, 1207–1224 (2019).
32. Han, X. et al. High coastal eddy activity around Antarctica revealed by SWOT. *National Science Review*. nwag181, https://doi.org/10.1093/nsr/nwag181 (2026).
33. Fu, L. et al. The surface water and ocean topography mission: a breakthrough in radar remote sensing of the ocean and land surface water. *Geophys. Res. Lett.* **51**, e2023GL107652 (2024).
34. Wang, J. et al. SWOT mission validation of sea surface height measurements at sub-100 km scales. *Geophys. Res. Lett.* **52**, e2025GL114936 (2025).
35. Ballarotta, M. et al. On the resolutions of ocean altimetry maps. *Ocean Sci.* **15**, 1091–1109 (2019).
36. Nurser, A. J. G. G. & Bacon, S. The Rossby radius in the Arctic Ocean. *Ocean Sci.* **10**, 967–975 (2014).
37. Spall, M. A., Pickart, R. S., Fratantoni, P. S. & Plueddemann, A. J. Western Arctic shelfbreak eddies: formation and transport. *J. Phys. Oceanogr.* **38**, 1644–1668 (2008).
38. Von Appen, W.-J. & Pickart, R. S. Two configurations of the Western Arctic shelfbreak current in summer. *J. Phys. Oceanogr.* **42**, 329–351 (2012).
39. Pickart, R. S., Weingartner, T. J., Pratt, L. J., Zimmermann, S. & Torres, D. J. Flow of winter-transformed Pacific water into the Western Arctic. *Deep Sea Res. Part II: Topical Stud. Oceanogr.* **52**, 3175–3198 (2005).
40. Watanabe, E. Beaufort shelf break eddies and shelf-basin exchange of Pacific summer water in the western Arctic Ocean detected by satellite and modeling analyses. *J. Geophys. Res.* **116**, C08034 (2011).
41. Huang, J., Pickart, R. S., Foukal, N., Spall, M. A. & Lin, P. Structure and variability of the Barrow Canyon outflow from two high-resolution shipboard surveys in 2018. *JGR Oceans* **128**, e2023JC019640 (2023).
42. Li, S. et al. Upwelling of Atlantic Water in Barrow Canyon, Chukchi Sea. *JGR Oceans* **127**, e2021JC017839 (2022).
43. Nghiem, S. V., Hall, D. K., Rigor, I. G., Li, P. & Neumann, G. Effects of Mackenzie River discharge and bathymetry on sea ice in the Beaufort Sea. *Geophys. Res. Lett.* **41**, 873–879 (2014).
44. Lin, P., Pickart, R. S., Pisareva, M. & Williams, B. Upper-layer circulation at the mouth of Amundsen Gulf, Arctic Ocean. *Prog. Oceanogr.* **235**, 103491 (2025).
45. Sévigny, C., Gratton, Y. & Galbraith, P. S. Frontal structures associated with coastal upwelling and ice-edge subduction events in southern Beaufort Sea during the Canadian Arctic Shelf Exchange Study. *JGR Oceans* **120**, 2523–2539 (2015).
46. Timmermans, M.-L., Toole, J., Proshutinsky, A., Krishfield, R. & Plueddemann, A. Eddies in the Canada Basin, Arctic Ocean, observed from ice-tethered profilers. *J. Phys. Oceanogr.* **38**, 133–145 (2008).
47. Dibarboure, G. et al. Data-driven calibration algorithm and pre-launch performance simulations for the SWOT mission. *Remote Sens.* **14**, 6070 (2022).
48. Dibarboure, G. et al. Blending 2D topography images from the Surface Water and Ocean Topography (SWOT) mission into the altimeter constellation with the Level−3 multi-mission Data Unification and Altimeter Combination System (DUACS). *Ocean Sci.* **21**, 283–323 (2025).
49. Tréboutte, A. et al. KaRIn noise reduction using a convolutional neural network for the SWOT ocean products. *Remote Sens.* **15**, 2183 (2023).
50. Nilsson, B., Andersen, O. B. & Knudsen, P. Assessment of the Performance of SWOT for Observing the Static Ocean Topography. *Geophys. Res. Lett.* **52**, (2025).
51. Charayron, R. et al. Blending data from SWOT KaRIn science phase and 30 years of nadir altimetry to improve Mean Sea Surface models. https://meetingorganizer.copernicus.org/EGU25/EGU25-8570.html (2025).
52. Schaeffer, P. et al. The CNES CLS 2022 Mean Sea Surface: Short Wavelength Improvements from CryoSat-2 and SARAL/AltiKa High-Sampled Altimeter Data. *Remote Sens.* **15**, 2910 (2023).
53. Laloue, A. et al. Merging Recent Mean Sea Surface Into a 2023 Hybrid Model (From Scripps, DTU, CLS, and CNES). *Earth Space Sci.* **12**, e2024EA003836 (2025).
54. Droghei, R., Buongiorno Nardelli, B. & Santoleri, R. A new global sea surface salinity and density dataset from multivariate observations (1993–2016). *Front. Mar. Sci.* **5**, 84 (2018).
55. Buongiorno Nardelli, B., Droghei, R. & Santoleri, R. Multi-dimensional interpolation of SMOS sea surface salinity with surface temperature and in situ salinity data. *Remote Sens. Environ.* **180**, 392–402 (2016).
56. Ubelmann, C. et al. Simultaneous estimation of ocean mesoscale and coherent internal tide sea surface height signatures from the global altimetry record. *Ocean Sci.* **18**, 469–481 (2022).
57. Ubelmann, C. et al. Reconstructing Ocean Surface Current Combining Altimetry and Future Spaceborne Doppler Data. *JGR Oceans* **126**, e2020JC016560 (2021).
58. Uprety, S. et al. Radiometric Intercomparison between Suomi-NPP VIIRS and Aqua MODIS Reflective Solar Bands Using Simultaneous Nadir Overpass in the Low Latitudes. *J. Atmos. Ocean. Technol.* **30**, 2720–2736 (2013).
59. Cao, C. et al. Suomi NPP VIIRS sensor data record verification, validation, and long-term performance monitoring. *JGR Atmos.* **118**, (2013).
60. Cao, C., De Luccia, F. J., Xiong, X., Wolfe, R. & Weng, F. Early on-orbit performance of the visible infrared imaging radiometer suite onboard the Suomi National Polar-Orbiting Partnership (S-NPP) satellite. *IEEE Trans. Geosci. Remote Sens.* **52**, 1142–1156 (2014).
61. Madec, G., & the NEMO Team. (2016). NEMO ocean engine. (Note du Pôle de modélisation). Institut Pierre-Simon Laplace (IPSL, 2016).
62. Fichefet, T. & Maqueda, M. A. M. M. Sensitivity of a global sea ice model to the treatment of ice thermodynamics and dynamics. *J. Geophys. Res. Oceans* **102**, 12609–12646 (1997).
63. Iovino, D., Vancoppenolle, M. & Fichefet, T. Implementation of LIM Sea Ice Model in the CMCC Global Ocean High-Resolution Configuration. *Research Papers Issue RP02092013* (2013).
64. Masina, S. et al. An ensemble of eddy-permitting global ocean reanalyses from the MyOcean project. *Clim. Dyn.* **49**, 813–841 (2017).
65. Hersbach, H. et al. The ERA5 global reanalysis. *Q. J. R. Meteorol. Soc.* **146**, 1999–2049 (2020).
66. Egbert, G. D. & Erofeeva, S. Y. Efficient inverse modeling of barotropic ocean tides. *J. Atmos. Ocean. Technol.* **19**, 183–204 (2002).
67. Bamber, J., Van den Broeke, M., Ettema, J., Lenaerts, J. & Rignot, E. Recent large increases in freshwater fluxes from Greenland into the North Atlantic. *Geophys. Res. Lett.* **39**, L19501 (2012).
68. Dai, A., Qian, T., Trenberth, K. E. & Milliman, J. D. Changes in continental freshwater discharge from 1948 to 2004. *J. Clim.* **22**, 2773–2792 (2009).
69. Dai, A. & Trenberth, K. E. Estimates of freshwater discharge from continents: latitudinal and seasonal variations. *J. Hydrometeorol.* **3**, 660–687 (2002).

70. Blanke, B. and Delecluse, P. Variability of the tropical Atlantic Ocean simulated by a general circulation model with two different mixed-layer physics. *J. Phys. Oceanograph.* 1363–1388 (1993).
71. Ni, Q., Zhai, X., Wang, G. & Marshall, D. P. Random movement of mesoscale eddies in the global ocean. *J. Phys. Oceanogr.* **50**, 2341–2357 (2020).
72. Qiu, B., Chen, S., Wang, J. & Fu, L. Seasonal and fortnight variations in internal solitary waves in the Indonesian Seas from the SWOT measurements. *JGR Oceans* **129**, e2024JC021086 (2024).
73. Hui, Y., Zhang, L., Sasaki, H., Wang, F. & Hu, D. Spatiotemporal features and generation mechanisms of submesoscale processes in the low-latitude Western Pacific Ocean. *J. Phys. Oceanograph.* (2025).
74. Müller, V., Kieke, D., Myers, P. G., Pennelly, C. & Mertens, C. Temperature flux carried by individual eddies across 47°N in the Atlantic Ocean. *J. Geophys. Res. Oceans* **122**, 2441–2464 (2017).
75. Yang, Y., Zeng, L., Wang, Q., Shi, R. & Xiu, P. Imprints of eddy stirring and trapping effects on global salt transport. *Earth's. Future* **13**, e2024EF005330 (2025).
76. Li, D., Wei, H. & Ruan, X. The importance of eddy stirring in wind-driven coastal upwelling. *J. Phys. Oceanogr.* **55**, 29–42 (2025).

Acknowledgements

We gratefully acknowledge the Digital Research Alliance of Canada (alliancecan.ca) for supplying the computational resources required for performing and archiving all model experiments. We also thank Qinbiao Ni for providing the original eddy detection code. Funding. QW discloses support for the research of this work from the German Helmholtz Climate Initiative REKLIM and the AWI INSPIRES program. C.F. discloses support for the research of this work from the Canadian Ocean Modelling Forum Workshop Funding, Mitacs Globalink (FR157603), and the Chinese Scholarship Council (202208180005). X.H. and C.P. declare no relevant funding. P.M. discloses support for the research of this work from the Natural Sciences and Engineering Research Council (NSERC) of Canada (rgpin227438-09).

Author contributions

Q.W. and C.F. designed the study; C.F. and X.H. modified the eddy detection code; C.P. and P.M. developed the regional high-resolution NEMO simulation; C.F. conducted data analysis and visualization, and wrote the original manuscript; Q.W. and C.F. interpreted and discussed the results, and both contributed to further manuscript edits.

Funding

Open Access funding enabled and organized by Projekt DEAL.

Competing interests

The authors declare no competing interests.

Additional information

Supplementary information The online version contains supplementary material available at https://doi.org/10.1038/s43247-026-03498-9.

Correspondence and requests for materials should be addressed to Qiang Wang.

Peer review information *Communications Earth and Environment* thanks Minghai Huang and the other anonymous reviewer(s) for their contribution to the peer review of this work. Primary Handling Editors: Jennifer Veitch and Alice Drinkwater. A peer review file is available.